

**The Impact of NASA Global Hawk Unmanned Aircraft Dropwindsonde Observations on
Tropical Cyclone Track, Intensity, and Structure: Case Studies**

Hui Christophersen

University of Miami/Cooperative Institute for Marine and Atmospheric Studies, Miami, Florida

Altug Aksoy

University of Miami/Cooperative Institute for Marine and Atmospheric Studies, Miami, Florida

Jason Dunion

University of Miami/Cooperative Institute for Marine and Atmospheric Studies, Miami, Florida

Kathryn Sellwood

University of Miami/Cooperative Institute for Marine and Atmospheric Studies, Miami, Florida

Submitted to Monthly Weather Review

Corresponding author address: Hui Christophersen,
CIMAS, Rosenstiel School of Marine and Atmospheric Science, 4600 Rickenbacker Cswy., Miami, FL 33149.
Email: hui.christophersen@noaa.gov

Abstract

The impact of Global Hawk dropwindsondes on tropical cyclone analyses and forecasts is evaluated in an ensemble-based vortex-scale data assimilation system. Two cases from Hurricane Edouard (2014) are presented. In the first case, inner-core observations were exclusively provided by Global Hawk (GH) dropwindsondes, while in the second case, GH dropwindsondes were concentrated in the storm's near environment and were complemented by an extensive number of inner-core observations from other aircraft. It is found that when GH dropwindsondes are assimilated, a positive impact on the minimum sea-level pressure (MSLP) forecast persists for most lead times in the first case, conceivably due to the better representation of the initial vortex structure, such as the warm-core anomaly and primary and secondary circulations. The verification of the storm's kinematic and thermodynamic structure in the forecasts of the first case is carried out relative to the time of the appearance of a secondary wind maximum (SWM) using the tail Doppler radar and dropwindsonde composite analyses. A closer-to-observed wavenumber-zero wind field in the experiment with GH dropwindsondes is seen before the SWM is developed, which likely contributes to the superior intensity forecast up to 36 h. The improvement in the warm-core anomaly in the forecasts from the experiment with GH dropwindsondes is believed to have also contributed to the consistent improvement in the MSLP forecast. For the latter case, a persistent improvement in the track forecast is seen, which is consistent with a better representation of the near-environmental flow obtained from GH data in the same region.

1. Introduction

Unmanned aircraft systems (UAS) have emerged as an alternative method of collecting weather observations to improve understanding of the tropical cyclone (TC) environment and the accuracy of TC forecasts (Braun et al. 2016; Cione et al. 2016), particularly in hazardous conditions where it is too dangerous to operate manned reconnaissance aircraft. The Global Hawk (GH) is one such aircraft that can fly for up to 24 h at an altitude of 60,000 ft and was first deployed by NASA during its Genesis and Rapid Intensification Processes (GRIP) experiment (Braun et al. 2013), followed by the Hurricane and Severe Storm Sentinel (HS3) project (2012-2014; Braun et al. 2016). Subsequently, the National Oceanic and Atmospheric Administration's (NOAA) Sensing Hazards with Operational Unmanned Technology (SHOUT) project began to deploy the GH in 2015 to investigate high-impact weather events (Black et al. 2014).

The GH is equipped with a suite of instruments capable of collecting both TC inner-core ($R \leq \sim 150$ km, where R denotes distance from storm center; Rogers et al. 2012) and environmental measurements ($R \sim 150$ -500 km). For the NOAA SHOUT program, the GH payload is configured to include GPS dropwindsondes (Hock and Franklin 1999), also used in HS3, the NASA High-Altitude Imaging Wind and Rain Airborne Radar (HIWRAP, Heymsfield et al., 2013) conically scanning Doppler radar, and the High Altitude MMIC Sounding Radiometer (HAMSR, Brown et al., 2013) along-track microwave sounder. The present study exclusively focuses on dropwindsondes. The GH can deploy up to 90 dropwindsondes per mission, providing high-vertical-resolution profiles of pressure, temperature, humidity and winds (Hock and Franklin 1999).

Earlier studies have found that the assimilation of dropwindsondes from traditional manned reconnaissance aircraft (e.g., the NOAA WP-3D Orion, P-3) generally leads to

improvements in TC track (Aberson and Franklin 1999; Chou et al. 2011; Majumdar et al. 2013) and intensity (Aberson and Franklin 1999; Torn 2014) forecasts in global and regional modeling applications. Compared to traditional aircraft, the GH offers much longer range and higher-altitude sampling. GH dropwindsondes deployed in Hurricane Edouard (2014) were used to examine the storm's thermodynamic and kinematic structures (Zawislak et al. 2016; Rogers et al. 2016). These observational studies demonstrate the value of high-altitude dropwindsondes. However, studies on the impact of high-altitude dropwindsondes on TC analyses and forecasts at the vortex scale that are relevant for TC inner-core processes (e.g., primary/secondary circulations, warm core, eyewall convection) are sparse. With this motivation, the present study investigates the impacts of GH dropwindsondes in a high-resolution TC analysis and forecast system. Results from case studies are presented, with cases carefully selected to represent potential operational settings and compare the scenarios of simultaneous manned and unmanned aircraft missions (possible when a storm is within range of manned aircraft) versus unmanned missions only (when a storm is away from land and out of range for manned aircraft). Section 2 briefly describes the cases, the data assimilation (DA) and modeling system, as well as the experimental setup. Results are shown in Section 3 to 5. A brief summary is presented in the last section.

2. Data and Experiments

2.a. Description of the cases

Hurricane Edouard (2014) was a North Atlantic TC that was intensively sampled by NASA and NOAA aircraft. Peak intensity of Edouard occurred at 1200 UTC on 16 September with the maximum sustained 10-m wind speed of 105 kt (54 m s^{-1}) (Stewart 2014). During Edouard's life cycle, NASA conducted four GH missions and NOAA flew eight P-3 missions

and one mission with the Gulfstream IV-SP (G-IV) aircraft. The case studies featured here are 0600 UTC 15 September during its intensification stage and 1800 UTC 16 September during its eyewall replacement cycle (ERC).

2.b. Data Assimilation System: HEDAS

The Hurricane Ensemble Data Assimilation System (HEDAS) combines an ensemble Kalman filter (EnKF; Whitaker and Hamill 2002), NOAA's Hurricane Weather Research and Forecast (HWRF) modeling system (Gopalakrishnan et al. 2012), and a storm-relative observation processing capability (Aksoy 2013). It is a research system that is specifically designed to assimilate high-resolution TC inner-core observations at the vortex scale. HEDAS has been used to assess the impact of a wealth of reconnaissance data and satellite retrievals for TCs both with simulated (Aksoy et al. 2012) and real (Aksoy et al. 2013; Aberson et al. 2015) datasets, producing realistic TC vortex analyses and statistically significant improvements in TC track and intensity forecasts.

2.c. Experiment setup

To evaluate the impact of GH dropwindsondes, HEDAS is run with all available observations (experiment “All”) and with GH dropwindsondes withheld from DA (experiment “noGH”). The GH dropwindsonde impact is then assessed from the differences between these two experiments.

During DA, a 30-min cycling frequency is used. Covariance inflation is appropriately tuned to account for sampling and modeling errors; 50% covariance relaxation (Zhang et al. 2004) and 5% prior covariance inflation (Hamill and Whitaker 2005) are applied. The covariance localization length scale of GH dropwindsondes is treated similarly to the dropwindsondes from the P-3 and G-IV (Aksoy et al. 2013; Aberson et al. 2015). All observations are processed in a

storm-relative framework (Aksoy 2013) at 3-km grid spacing. HEDAS uses the first 30 (out of 80) ensemble members from NOAA’s EnKF-based Global Forecast System (GFS) analyses (Hamill et al. 2011) as the initial/boundary conditions during the initial spin-up and DA. Detailed DA and model configurations are listed in Table 1.

3. Data Distribution for the Two Cases

Standard reconnaissance observations are assimilated. These include tail Doppler radar (TDR) wind velocity superobservations (superobs; Gamache 2005), GPS dropwindsondes (Hock and Franklin 1999) at both significant and standard pressure levels (wind speed, temperature, and specific humidity), flight-level high-density observations of wind speed, temperature and specific humidity at 30-s interval, and 10-m wind speed retrievals from the Stepped Frequency Microwave Radiometer (SFMR; Uhlhorn et al. 2007). Satellite retrievals such as atmospheric motion vectors (AMVs; Velden et al. 2005) and cloud-cleared retrievals of temperature and specific humidity from the Atmospheric Infrared Sounder (AIRS; Susskind et al. 2003) are also included in the two cases.

It should be noted that hereafter, an “observation” signifies a single measurement of temperature, specific humidity, or the zonal/meridional component of wind at a specific geographic location, pressure level, and time.

Figure 1 shows the spatial distribution of assimilated observations for the two cases considered. In the first case, within the six-hour window centered around 0600 UTC 15 September, there are 4,097 wind observations (23% from GH) and 4,116 thermodynamic observations (20% from GH) in total. On this day, the inner core of the storm was exclusively sampled by the GH dropwindsondes, extending in coverage vertically to an altitude of 16 km (Figs. 1a-c).

For the 1800 UTC 16 September case, there are a total of 54,608 wind (only 5% from GH dropwindsondes because of high volume of NOAA P-3 TDR superobs) and 5,644 thermodynamic observations (28% from GH) that are assimilated (Figs. 1d-e). For this case, although small in relative numbers, GH inner-core dropwindsondes complement their NOAA P-3 counterparts at higher altitudes, providing enhanced temporal sampling and extended radial sampling (radially to ~500 km from storm center, Fig. 1f). The GH dropwindsonde observations were distributed approximately uniformly out to 500 km radius from the storm center (Figs. 1d-f).

It should be noted that HEDAS accounts for dropwindsonde horizontal drift (Aberson et al. 2015; Aksoy et al. 2013), which can be quite large in the high-wind-speed regions. It is therefore important to assimilate observations at accurate locations at each pressure level so that the adjustments to the background are reasonable. HEDAS assimilates dropwindsondes both at the significant and mandatory pressure levels, contributing to the uneven density distribution vertically (Figs. 1c, 1f). Furthermore, a recently discovered dry bias issue for dropwindsonde observations above 400 hPa (Vömel et al. 2016) is not expected to have significant impact on current analyses and forecasts, because a constant observation error standard deviation for specific humidity of 0.5 g kg^{-1} is assigned regardless of model vertical level. This error is large compared to the small magnitudes of specific humidity typically found in the upper troposphere, thus significantly limiting the impact of humidity observations there on the model state variables.

4. Impact of GH Dropwindsondes on TC Analyses and Forecasts

4.a. Kinematic and thermodynamic analyses

The impact of GH dropwindsondes is first examined with respect to final analyses. Fig. 2a-c indicates that on 15 September 0600UTC the storm has much stronger intensity (i.e., maximum 10-m sustained surface wind speed) as a result of assimilating GH dropwindsondes.

The location of the maximum 10-m wind speed shifts from the north of the storm center in experiment noGH to the east in All. With the assimilation of GH dropwindsondes, the intensity is around 42 m s^{-1} (Fig. 2a), close to the Best Track intensity of 44 m s^{-1} . Meanwhile, the corresponding experiment noGH only has an intensity of 30 m s^{-1} (Fig. 2b). In addition, the assimilation of GH dropwindsondes results in a slight shift in the location of the storm center (Figs. 2a-b), with the position in All that better matches the Best Track position than in the noGH experiment. Accounting for this center shift, the All-noGH wind speed differences are up to 20 m s^{-1} near the eyewall region (Fig. 2c), conceivably both from changes in the radius of the maximum wind (RMW; also see Fig. 3) and intensity.

On 16 September 1800UTC, wind speed differences of $1\text{-}3 \text{ m s}^{-1}$ are seen near the storm center as well as in the near-storm environment (Fig. 2f). Despite the predominant coverage of P-3 TDR wind observations in the inner-core region and AMV and AIRS in the storm environment (Fig. 1d,e), GH dropwindsondes still show some impact in the vicinity of the storm center and away from the storm center (Fig. 2f). We note that the ratio of the absolute analysis increments for the inner-core region relative to the near-storm environment is greater than 5 for the first case, but only about 1.8 for the second case. Therefore, relative to the inner core, the impact on the storm environment as a result of assimilating GH dropwindsondes is greater in the second case than in the first case.

The assimilation of GH dropwindsondes also influences the primary and secondary circulation structures. Figure 3 shows the azimuthally averaged tangential wind speed on 15 and 16 September. A much stronger, deeper, and more compact vortex is seen on 15 September in experiment All compared to noGH. Tangential wind speed differences greater than 7 m s^{-1} are seen within 100 km of the center extending vertically up to 12 km, which is largely attributed to

the exclusiveness of GH dropwindsondes in the inner core. Particularly noteworthy is the impact of GH dropwindsondes on inner-core wind analyses between 8 and 12 km. This is a region that NOAA operational aircraft do not sample well due to safety restrictions of the G-IV aircraft. The storm in experiment All also exhibits a stronger secondary circulation (radial inflow and outflow, Figs. 3 a-c). Meanwhile on 16 September, Figs. 3d-f suggest that comparable tangential wind speed analysis increments ($1-3 \text{ m s}^{-1}$) exist both near the storm center and away from it. This impact is in stark contrast to the 15 September case where the greatest impact is in the inner core. For the case of 16 September, GH dropwindsondes do not result in any large differences in the inner-core secondary circulation (Fig. 3d-f).

The impact of GH dropwindsondes on the thermodynamic fields is also examined. Figure 4 shows the azimuthally averaged temperature anomaly (relative to analyzed temperature at a radius of 300-700 km away from the center, Stern and Zhang 2016) and relative humidity. The height of the maximum temperature anomaly on 15 September is around 8 km. The storm in experiment All has a much stronger warm-core anomaly and a much moister upper-level core (Figs. 4a-c). GH dropwindsondes also result in slightly drier near storm environmental air for this case (Fig. 4c). Compared to 15 September, the warm-core anomaly height on 16 September is higher (at 9 km) but slightly weaker. However, the experiments All and noGH on 16 September do not indicate any large inner-core thermodynamic differences (Figs. 4d-f), presumably because the indirect update from assimilating the large volume of TDR wind observations overwhelms the assimilation of the few direct thermodynamic measurements from dropwindsondes. Although the TDR update is indirect, correlations between wind and temperature in the warm-core regions of mature hurricanes are typically strong (e.g., Poterjoy and Zhang 2011).

4.b. Verification of track and intensity in deterministic forecasts

The deterministic forecast errors computed relative to the Best Track estimates (Jarvinen et al. 1984) are shown in Fig. 5. On 15 September, the intensity forecast shows an improvement in experiment All for short lead times (up to 36 h), while improvements for the minimum sea-level pressure (MSLP) are consistent across all lead times. The track forecast from the experiment All also demonstrates a marginal yet consistent improvement. The consistent MSLP improvement is attributed to the better sampling of the inner-core vortex and the resulting improvements in the kinematic and thermodynamic structures, as previously discussed.

In marked contrast to the 15 September case, on 16 September, large improvements in the track forecast are evident, especially for long lead times along with marginal impact on intensity. The noticeable impact of GH dropwindsondes on the storm's near-environment is believed to contribute to the track improvement. The mid-level wind field in the GH experiment shows a stronger northerly component to the north of the storm and a stronger easterly component to the south (not shown). These differences slow down the translation speed of the vortex to keep it further south, closer to the observed track.

4.c. Verification of TC structure in deterministic forecasts

Figure 6 shows Hovmoller diagrams of the forecasts of azimuthally averaged tangential wind speed, total cloud water content, and vertical wind speed at 3-km altitude for the first case (0600 UTC 15 September). The appearance of a secondary wind maximum is clearly represented by strong vertical velocities and total cloud water content in experiment All at around 27 h, resulting in a temporary weakening of MSLP (Fig. 6d). The RMW at 1-km altitude also increases followed by the wind field expansion. The secondary eyewall propagates inward (Figs. 6b-c) as the tangential wind speed expands radially (Fig. 6a). The completion of the ERC is

followed by re-intensification of tangential wind field at around 54 h, but the RMW of the storm doesn't contract, as would be typically observed in ERC (Sitkowski et al. 2011).

By contrast, in the experiment noGH, a similar expansion of the tangential wind field (albeit with smaller magnitude of wind speed) is seen at the lead time of around 36 h, but with less total cloud water content and less vigorous vertical velocity than in All. The MSLP evolution in the noGH experiment does not depict as clear an ERC cycle as in the experiment All. It is noted, however, that the timing of the appearance of the second wind maximum in the two experiments is also different. The All experiment is initialized with a much stronger, deeper and more compact vortex than the one in noGH (Fig. 3 and Fig. 4), and hence it is likely that this contributes to the earlier appearance of the secondary wind maximum in All than in noGH. Furthermore, the intensification/weakening/re-intensification stages also evolve much faster in both of the experiments compared to a typical ERC process (Sitkowski et al. 2011).

During the period 15-17 September that encompasses both of the cases investigated when Hurricane Edouard underwent near-rapid intensification followed by an ERC period (Stewart 2014; Abraca 2016; Zawislak et al. 2016; Rogers et al. 2016), there were three back-to-back NOAA missions with the P-3 aircraft, one NOAA mission with the G-IV aircraft, and two NASA missions with the GH (http://www.aoml.noaa.gov/hrd/Storm_pages/edouard2014/mission.html). For suitable comparison between observed and predicted vortex structures, appropriate forecast lead times are chosen when the secondary wind maximum appears in respective experiments (around 1000 UTC 16 September for All and 1800 UTC for noGH, as indicated with black dashed lines in Fig. 6) to match the time of the aircraft observations when the double-eyewall structure was apparent (1800 UTC 16 September). Hereafter, the appearance of the forecast and observed secondary

wind maxima will be denoted as “FSWM” and “OSWM”, respectively. Similarly, verification is also carried out for the other two times when aircraft observations are available 24 h before OSWM (1800 UTC 15 September) and 21 h after OSWM (1500 UTC 17 September) by choosing lead times relative to FSWM (i.e., FSWM minus 24 h and FSWM plus 21 h).

Figure 7 shows the three composite TDR wind analyses from all available aircraft for the three observation times mentioned. At OSWM - 24 h (Fig. 7 a-c), the experiment All has an eyewall slope that better matches the observed than in noGH. The RMW of the vortex in All is around 50 km, similar to what TDR observed, while the RMW in no GH is at around 60 km. The vortex in All is also deeper than in noGH, and more similar to the observed vortex. It is hypothesized that these improvements in the All structure are then reflected in the short-range (0-36 h) improvements of forecast Vmax error as compared to noGH (Fig. 5).

At 1800 UTC 16 September (OSWM), the vortex has started to form a secondary wind maximum (Fig. 7d), and by 1500 UTC 17 September, the outer eyewall has become well defined and the inner eyewall has nearly collapsed (Fig. 7h). At the second verification time of the TDR composite analysis (FSWM), the vortex in both experiments shows an expansion of the tangential wind field at 3 km altitude. There is a deeper and stronger low-level (at an altitude of 2-4 km) radial outflow associated with the secondary wind maximum in experiment All than in noGH (Fig. 7e-f). Compared to the corresponding TDR composite analysis (Fig. 7d) where the secondary wind maximum appears at a radius of around 120-140 km, both experiments develop their respective secondary wind maxima at a radius of around 100-120 km (Fig. 7e-f).

At FSWM + 21 h, although both experiments seem to capture the outer eyewall (Fig. 7 i-j), neither of them has the presence of the weak inner eyewall as observed in the TDR analysis (Fig. 7h). Therefore, from the lead time of FSWM onward, both All and noGH experiments

present similar kinematic wavenumber-0 structures, with the vortex in noGH slightly weaker than in All and closer in magnitude to observed. This likely contributes to the smaller Vmax errors in noGH than All beyond the forecast lead time of 36 h (Fig. 5).

Similarly, the thermodynamic structure from the deterministic forecasts is verified against a dropwindsonde composite analysis from both NOAA and NASA missions, centered at OSWM +/- 3 h. The radial dropwindsonde distribution that contributes to this composite analysis can be found in Zawislak et al. (2016). Specifically, Figure 8 shows the azimuthal means of the warm-core anomaly (as obtained by subtracting the azimuthally averaged near-environment temperature profiles 300-700 km away from the storm center, Stern and Zhang 2016) and relative humidity for both experiments at their respective lead times of FSWM and for dropwindsondes at the time of OSWM. The forecast fields in both experiments show the height of the maximum temperature anomaly at around 8 km (Fig. 8a-b), while the dropwindsonde composite depicts the height of the maximum temperature anomaly at an altitude of 8-10 km (Fig. 8c). Particularly, the temperature anomaly structure in All is closer to what dropwindsondes observed within a radius of ~30 km at mid-levels (6-10 km altitude) than noGH (Fig. 8a-c). For relative humidity, both experiments greatly underestimate the moisture content in the upper levels of the vortex core, forecasting a much dryer upper vortex than actually observed. However, considering that the corresponding HEDAS analysis (verifying at the same time as the dropwindsonde composite) presents a very realistic humidity structure (Fig. 8d), we deduce that the upper-level dry bias in the forecasts is due to model error rather than data assimilation itself. Nonetheless, the overall wavenumber-0 thermodynamic structure in All is slightly superior to noGH, which also likely contributes to the consistent improvements in MSLP forecast in All for the case of 0600 UTC 15 September (Fig. 5).

5. On the impact of the NOAA P-3 data for the case of 1800 UTC 16 September

We note that there were inner-core NOAA P-3 reconnaissance observations available for the second case (1800 UTC 16 September), but not for the first case (0600 UTC 15 September). Therefore, for completeness, a third experiment is carried out for the second case where P-3 reconnaissance observations are not assimilated so that the impact of GH dropwindsondes can be clearly deduced similar to the first case. However, without the NOAA P-3 data, it is found that the analyzed vortex does not represent the complex double-eyewall structure (Fig. 9) as observed by the TDR data (Fig. 7d). We believe that the coverage and resolution of the P-3 TDR data were critical in this case to obtain the secondary wind maximum in the analysis, especially because the GFS backgrounds that HEDAS analyses are spun up from are not expected to be capable of representing such complex structures well (not shown); the GH dropwindsondes alone were not able to provide the comparable information content for wind structure (especially in the radial direction). In contrast, in the first case, the storm presented a typical mature hurricane kinematic structure with a single eyewall, and the coverage and spacing of GH dropwindsondes were adequate to significantly reduce analysis and forecast errors (Fig. 5) in this situation. Hence, we conclude that the impact of inner-core dropwindsondes should not be expected to be comparable in all hurricane cases, which suggests that sampling strategies may have to be modified to account for the variability in the complexity of vortex structures. Obviously, more case studies are needed to verify this hypothesis.

6. Conclusions and Discussion

The two cases from Hurricane Edouard (2014) present unique data distributions that reveal the potential strengths of GH dropwindsonde sampling in hurricanes. Specifically, in the first case (0600 UTC 15 September), the GH dropwindsondes provided nearly all inner-core

wind and thermodynamic observations, while in the latter case (1800 UTC 16 September), the GH dropwindsondes were accompanied by a large volume of data from other NOAA aircraft but remained mostly concentrated in the storm's near-environment compared to the first case (except for some AMV and AIRS observations at larger radii). These case studies demonstrate the potential impacts of assimilating GH dropwindsondes at the vortex scale.

As a result of these dropwindsonde distributions relative to data from other platforms, we see large impacts from assimilating GH dropwindsondes on the kinematic and thermodynamic analyses in the inner-core region for the 0600 UTC 15 September case. This leads to a better representation of the storm structure in terms of the warm-core anomaly and the primary and secondary circulations, which contributes to improved MSLP forecasts. In the 1800 UTC 16 September case, differences in model analyses with and without GH dropwindsondes are small in the inner core relative to the first case, but comparable analysis differences extend outward to the near-storm environment. The extensive suite of observations from other aircraft and satellite already contributes to the improved analysis in the inner-core structure. Nonetheless, the assimilation of GH dropwindsondes leads to a consistent track improvement for up to 5 days, which we attribute to the better representation of the near-storm environmental flow at initial time. It is noted that although the most noticeable analysis difference between the two cases is the dropwindsonde impact on the inner core, the ratio of the analysis increments in the inner core to environment also plays a role in modulating the overall vortex structure and the resulting deterministic forecast. Because of the different weights or relative impacts on the inner core and environment, we believe that the overall superior intensity forecast for the first case was mostly due to impact on the inner-core, while overall superior track forecast for the second case was largely due to impact on the environment.

Furthermore, since the deterministic forecast for the case of 0600 UTC 15 September in All is initiated from a much stronger, compact and deeper vortex than in noGH, the secondary wind maximum develops much faster in All than in noGH, accompanied with stronger indication of a secondary eyewall formation, as deduced from the precipitation and vertical velocity fields. We further use the timing of each experiment's forecast secondary wind maximum (FSWM) compared to their observed counterpart as a baseline for vortex structure verification. When the FSWM-relative kinematic structure is thus compared to the TDR observed secondary wind maximum (OSWM) structure, a closer-to-observed wavenumber-0 kinematic vortex structure is found in All than in noGH before the secondary wind maximum is developed, and this likely contributes to the superior intensity forecast in the short-range (0-36 h) forecast. A snapshot of the thermodynamic structure as obtained from a dropwindsonde composite analysis around the time of the OSWM is also compared to the forecast fields in both experiments. The vortex wavenumber-0 temperature anomaly structure in All is determined to be much closer to what dropwindsondes observed than in noGH. It is also noted, however, that the upper-level vortex near the inner core in both experiments is much dryer than either the dropwindsonde composite or the HEDAS analysis, suggesting that there are likely model processes that produce an upper-level dry bias during the forecasts.

We conclude that UAS observations, as exemplified by the GH dropwindsondes in the present study, complement observations obtained from manned surveillance missions, providing additional advantages of wider geographical range, longer temporal sampling, greater vertical extent, and high-resolution measurements. Our findings also provide some insights for designing flight patterns more strategically and synergistically depending on the availability of GH and traditional manned reconnaissance aircraft. For instance, when a storm is within range of the

NOAA P-3 aircraft, like in the second case, it is perhaps not the best use of resources to deploy the GH and P-3 dropwindsondes to both sample the inner core, since we have demonstrated that GH dropwindsondes may have greater relative contribution in the near-storm environment. Alternatively, when the storm is not within range of traditional manned aircraft as shown in the first case, it seems necessary for the GH to sample the inner core of the storm to obtain impact on storm intensity. However, one should bear in mind that GH dropwindsondes appear to have limitations in representing the inner-core complex structures compared to the P-3 equipped with the TDR capability. Clearly, further research is needed to identify how these findings would be modulated by availability of data from other observing platforms (land-based, airborne, or spaceborne) or factors that might influence storm structure such as storm lifecycle (e.g., genesis, rapid intensification, weakening and/or extratropical transition) and synoptic environment (e.g., vertical wind shear).

A caveat of our study is that results are based on individual cases. More cases are needed to obtain statistical significance and firm conclusions. For GH dropwindsondes, this is the subject matter of an ongoing study and the results will be reported elsewhere.

We further note that current results are obtained using HEDAS with proper tuning. They may vary in different DA and/or forecast systems depending on configuration, tuning, and types of observations assimilated. To address such variability, an ongoing study aims to compare the impact of GH dropwindsondes in HEDAS versus the operational HWRF DA system, the results of which will be reported in a later publication.

7. Acknowledgements

Authors acknowledge funding support from the NOAA UAS Program (Award number NA14OAR4830172). Insightful suggestions from Drs. Sim Aberson and Robert Rogers from

393 NOAA/AOML/HRD were very helpful to improve the manuscript. The data used in this study
394 were collected by the NASA HS3 field campaign, and are available at
395 https://espo.nasa.gov/hs3/content/HS3_0. This research was carried out under the auspices of
396 CIMAS, a joint institute of the University of Miami and NOAA (Cooperative Agreement
397 NA67RJ0149). Constructive comments from two anonymous peer reviewers have also greatly
398 improved the manuscript.

References:

- Aberson, S. D., and J. L. Franklin, 1999: Impact on hurricane track and Intensity Forecasts of GPS dropwindsonde observations from the first-season flights of the NOAA Gulfstream-IV Jet Aircraft. *Bull. Amer. Meteor. Soc.*, **80**, 421-427.
- , A. Aksoy, T. Vukicevic, K. J. Sellwood, and X. Zhang, 2015: Assimilation of high-resolution tropical cyclone observations with an ensemble Kalman filter using NOAA/AOML/HRD's HEDAS: Evaluation of the 2008-11 vortex-scale forecasts. *Mon. Wea. Rev.*, **143**, 511-523.
- Aksoy, A., 2013: Storm-relative observations in tropical cyclone data assimilation with an ensemble Kalman filter. *Mon. Wea. Rev.*, **41**, 506-522.
- , S. Lorsolo, T. Vukicevic, K. J. Sellwood, S. D. Aberson, and F. Zhang, 2012: The HWRF Hurricane Ensemble Data Assimilation System (HEDAS) for high-resolution data: the impact of airborne Doppler radar observations in an OSSE. *Mon. Wea. Rev.*, **140**, 1843-1862.
- , S. D. Aberson, T. Vukicevic, K. J. Sellwood, and X. Zhang, 2013: Assimilation of high-resolution tropical cyclone observations with an ensemble Kalman filter using NOAA/AOML/HRD's HEDAS: Evaluation of the 2008-11 vortex-scale analyses. *Mon. Wea. Rev.*, **143**, 511-523.
- Black M., G. A. Wick and R. E. Hood, 2014: Sensing hazards with operational unmanned technology: NOAA's multi-year plan to deploy the NASA Global Hawk aircraft for high impact weather, 31st Conference on Hurricanes and Tropical Meteorology, San Diego, CA.

420 Braun, S. A., P. A. Newman, and G. M. Heymsfield, 2016: NASA's Hurricane and Severe Storm
 421 Sentinel (HS3) investigation. *Bull. Am. Meteorol. Soc.*, 2085-2102, doi:10.1175/BAMS-D-
 422 15-00186.1.

423 Chou, K.-H., C.-C. Wu, P.-H. Lin, S. D. Aberson, M. Weissmann, F. Harnisch, and T.
 424 Nakazawa, 2011: The impact of dropwindsonde observations on typhoon track forecasts in
 425 DOTSTAR and T-PARC. *Mon. Wea. Rev.*, **139**, 1728-1743.

426 Cione, J. J., E. A. Kalina, E. W. Uhlhorn, A. M. Farber, and B. Damiano, 2016: Coyote
 427 unmanned aircraft system observations in Hurricane Edouard. *Earth Sp. Sci.*, 370-380.

428 Gamache, J. F., 2005: Final report on JHT project entitled: real-time dissemination of hurricane
 429 wind fields determined from airborne Doppler radar. [http://www.nhc.noaa.gov/jht/2003-
 430 2005reports/DOPLRgamache_JHTfinalreport.pdf](http://www.nhc.noaa.gov/jht/2003-2005reports/DOPLRgamache_JHTfinalreport.pdf)

431 Gopalakrishnan, S. G., S. Goldenberg, T. Quirino, X. Zhang, F. Marks, K.-S. Yeh, R. Atlas, and
 432 V. Tallapragada, 2012: Toward improving high-resolution numerical hurricane forecasting:
 433 Influence of model horizontal grid resolution, initialization, and physics. *Wea. Forecast.*,
 434 **27**, 647-666.

435 Hamill, T. M., J. S. Whitaker, D. T. Kleist, M. Fiorino, and S. J. Benjamin, 2011: Predictions of
 436 2010's tropical cyclones using the GFS and ensemble-based data assimilation methods.
 437 *Mon. Wea. Rev.*, **139**, 3243-3247.

438 Hock, T. F., and J. L. Franklin, 1999: The NCAR GPS Dropwindsonde. *Bull. Am. Meteorol.*
 439 *Soc.*, **80**, 407-420.

440 Jarvinen, B. R., C. J. Neumann, and M. A. S. Davis, 1984: A tropical cyclone data tape 475 for
 441 the North Atlantic basin, 1886–1983: Contents, limitations, and uses. NOAA Tech. 476
 442 Memo. NWS NHC 22, 21 pp.

443 Majumdar, S. J., M. J. Brennan, and K. Howard, 2013: The impact of dropwindsonde and
 444 supplemental rawinsonde observations on track forecasts for Hurricane Irene (2011). *Wea.*
 445 *Forecasting.*, **28**, 1385-1403.

446 Poterjoy, J., and F. Zhang, 2011: Dynamics and structure of forecast error covariance in the core
 447 of a developing hurricane. *J. Atmos. Sci.*, **68**, 1586-1606, doi:10.1175/2011JAS3681.1.

448 Rogers, R. F., S. Lorsolo, P. Reasor, J. Gamache, and F. Marks, 2012: Multiscale analysis of
 449 tropical cyclone kinematic structure from airborne Doppler radar composites. *Mon. Wea.*
 450 *Rev.*, **140**, 77-99.

451 ———, J. A. Zhang, J. Zawislak, H. Jiang, G. R. Alvey, Edward J Zipser, S. N. Stevenson, 2016:
 452 Observations of the structure and evolution of Hurricane Edouard (2014) during intensity
 453 change. Part II: Kinematic structure and the distribution of deep convection. *Mon. Wea.*
 454 *Rev.*, in press. doi: <http://dx.doi.org/10.1175/MWR-D-16-0017.1>.

455 Sitkowski, M., J. P. Kossin, and C. M. Rozoff, 2011: Intensity and structure changes during
 456 hurricane eyewall replacement cycles. *Mon. Wea. Rev.*, **139**, 3829-3847.

457 Stern, D. P., and F. Zhang, 2016: The warm-core structure of Hurricane Earl (2010). *J. Atmos.*
 458 *Sci.*, **73**, 3305–3328, doi:10.1175/JAS-D-15-0328.1.

459 Stewart, S. R., 2014: Tropical Cyclone Report, Hurricane Edouard 11-19 September 512 2014.
 460 Tropical Cyclone Report, National Hurricane Center, 19pp.

461 Susskind, J., C. D. Barnet, and J. M. Blaisdell, 2003: Retrieval of atmospheric and surface
 462 parameters from AIRS/AMSU/HSB data in the presence of clouds. *IEEE Trans. Geosci.*
 463 *Remote Sens.*, **41**, 390-409.

464 Torn, R. D., 2014: The impact of targeted dropwindsonde observations on tropical cyclone
 465 intensity forecasts of four weak systems during PREDICT. *Mon. Wea. Rev.*, **142**, 2860-
 466 2878.

467 Uhlhorn, E. W., P. G. Black, J. L. Franklin, M. Goodberlet, J. Carswell, and A. S. Goldstein,
 468 2007: Hurricane surface wind measurements from an operational Stepped Frequency
 469 Microwave Radiometer. *Mon. Wea. Rev.*, **135**, 3070–3085.

470 Velden, C.S., J. Daniels, D. Stettner, D. Santek, J. Key, J.P. Dunion, K. Holmlund, G. Dengel,
 471 W. Bresky, and W.P. Menzel, 2005: Recent innovations in deriving tropospheric winds
 472 from meteorological satellites. *Bull. Amer. Meteor. Soc.* **86**, 205-223.

473 Vömel, H., K. Young, and T. Hock, 2016: NCAR/EOL technical note: dropsondes dry bias.
 474 [Available online at
 475 [https://www.eol.ucar.edu/system/files/software/Aspen/Windows/W7/documents/Tech%20](https://www.eol.ucar.edu/system/files/software/Aspen/Windows/W7/documents/Tech%20Note%20Dropsonde_Dry_Bias_20160527_v1.3.pdf)
 476 [Note%20Dropsonde_Dry_Bias_20160527_v1.3.pdf](https://www.eol.ucar.edu/system/files/software/Aspen/Windows/W7/documents/Tech%20Note%20Dropsonde_Dry_Bias_20160527_v1.3.pdf)].

477 Whitaker, J. S., and T. M. Hamill, 2002: Ensemble data assimilation without perturbed
 478 observations. *Mon. Wea. Rev.*, **130**, 1913-1924.

479 Zawislak J., H. Jiang, G.R. Alvey III, E. J. Zipser, R. F. Rogers, J. A. Zhang, S. N. Stevenson,
 480 2016: Observations of the structure and evolution of Hurricane Edouard (2014) during
 481 intensity change. Part I: relationship between the thermodynamic structure and precipitation,
 482 *Mon. Wea. Rev.*, in press. doi: <http://dx.doi.org/10.1175/MWR-D-16-0018.1>.

483 Zhang, F., C. Snyder, and J. Sun, 2004: Impacts of initial estimate and observation availability
484 on convective-scale data assimilation with an ensemble Kalman filter. *Mon. Wea. Rev.*, **132**,
485 1238-1253.

486

LIST OF FIGURES:

Fig. 1: Spatial distribution of assimilated observations overlaid on visible satellite imagery for the experiment All (including all available observations) centered at (a-c) 0600 UTC 15 September and (d-f) at 1800 UTC 16 September for (a,d) wind observations and (b,e) thermodynamic observations. [Visible imagery courtesy of Naval Research Laboratory, Monterey, CA.] (c,f) Number of GH dropwindsonde observations (purple diamonds in the (a-b, d-e)) within a bin of 25 km in radius and 1 km in height.

Fig. 2: 10-m wind vectors (m s^{-1} , wind speed shaded) of the final analysis in the experiment All and noGH and their differences (All-minus-noGH, wind fields in the experiment noGH is aligned to the center of the experiment All) at 0600 UTC 15 September (a-c) and 1800 UTC 16 September (d-f). The difference of the wind speed is contoured at 0.5 m s^{-1} intervals (-6 to 6 m s^{-1}) and at 2 m s^{-1} intervals (6 to 20 m s^{-1}). Observed Best Track positions are also indicated in green hurricane symbol.

Fig. 3: Azimuthally averaged tangential wind speed (m s^{-1} , shaded) and radial wind speed (m s^{-1} , contours) of the final analysis from the experiment All (a,d) and noGH (b,e) and their differences (All-minus-noGH, c,f).

Fig. 4: As in Fig. 3 but for temperature anomaly (K, shaded) and relative humidity (% , contours).

Fig. 5: Track error, maximum sustained 10-m wind speed error (V_{max}), and minimum sea level pressure error (P_{min}) compared to the observed Best Track from the deterministic forecasts in the experiments All and noGH initialized at 0600 UTC 15 September (left panel) and 1800 UTC 16 September 2014 (right panel). Dashed lines indicate that the storm is a remnant low in the Best Track estimates.

Fig. 6: Radius-time Hovmoller diagrams of (a,e) azimuthally averaged tangential wind speed layer-averaged between 2.4-km and 3.5-km altitudes (shaded with additional black contours at 42 and 38 m s^{-1}), (b,f) total cloud water content condensate at 3-km altitude and (c,g) vertical velocity at 3-km altitude for the experiment All (a-c) and noGH (d-f) at hourly lead-time intervals initialized at 0600 UTC 15 September. The radius of maximum wind (RMW) at 1-km altitudes from both experiments are also shown in dark purple in (a-c) and (e-g). (d,h) Time evolution of the minimum sea level pressure (P_{min}) from the experiment All (blue line), noGH (red line), and the best track estimates (black line). The black dashed lines in (a-c) and (e-g) mark the appearance of forecast secondary wind maximum (FSWM). Their corresponding time of observed secondary wind maximum (OSWM) is also shown in black dashed circles (d,h).

Fig. 7: Azimuthal mean of tangential wind speed (m s^{-1} , shaded), radial wind speed (m s^{-1} , contours) and secondary circulation (m s^{-1} , vectors of radial winds and vertical velocity) around observed secondary wind maximum (OSWM) and forecast secondary wind maximum (FSWM), and 24 hour before and 21 hour later of the OSWM and FSWM for Hurricane Edouard.

Fig. 8: Azimuthally averaged temperature anomaly (K, shaded) and relative humidity (% , contours) from (a) the experiment All and (b) noGH initiated from the analysis of the first case at 0600 UTC 15 September at lead time when the appearance of forecast secondary wind maximum (FSWM) occurs, and (c) dropwindsonde composite ± 3 hour of 1800 UTC 16 September when observed secondary wind maximum (OSWM) occurs, and (d) the analysis of the secondary wind maximum (ASWM) from the case of 1800 UTC 16 September, 2014.

Fig. 9: Azimuthally averaged tangential wind speed (m s^{-1} , shaded) and radial winds (m s^{-1} , contours) from the analysis at 1800 UTC 16 September with P3 reconnaissance data denied.

Table 1: Summary of experiment setup.

	Feature	Setup
HEDAS	Cold-start initialization	Initialized from the first 30 GFS/EnKF analysis ensemble, 4-h spinup
	Filter type	Ensemble square root filter
	Observation processing	Storm relative
	Covariance relaxation (% prior)	50
	Covariance inflation (% prior)	5
	Covariance localization (grid points)	Through a compactly supported fifth-order correlation function, 60 grid point distance in the horizontal and 15 model levels in vertical
	Assimilation frequency	30 min
	Assimilation window	4 h (± 2 h relative to synoptic time)
	Assimilated observation types	Doppler radial velocity superobservations, dropwindsonde and flight-level wind speed, temperature and specific humidity, SFMR 10-m wind speed, AIRS retrievals, CIMSS AMV retrieved wind speed
HWRF	Model version	HWRF-Nonhydrostatic Mesoscale Model (NMM) core
	Resolution	Horizontal 9-km outer nest of approx. $60^\circ \times 60^\circ$ and 3-km vortex-following inner nest of approx. $10^\circ \times 10^\circ$; vertical 61 eta levels with model top 0.2 hPa
	Physics	Ferrier microphysics, simplified Arakawa-Schubert (SAS) cumulus (only in outer domain), GFDL surface layer plus GFDL land surface scheme, GFS PBL scheme with boundary surface roughness modified over ocean, GFDL radiation
	Ocean coupling	None

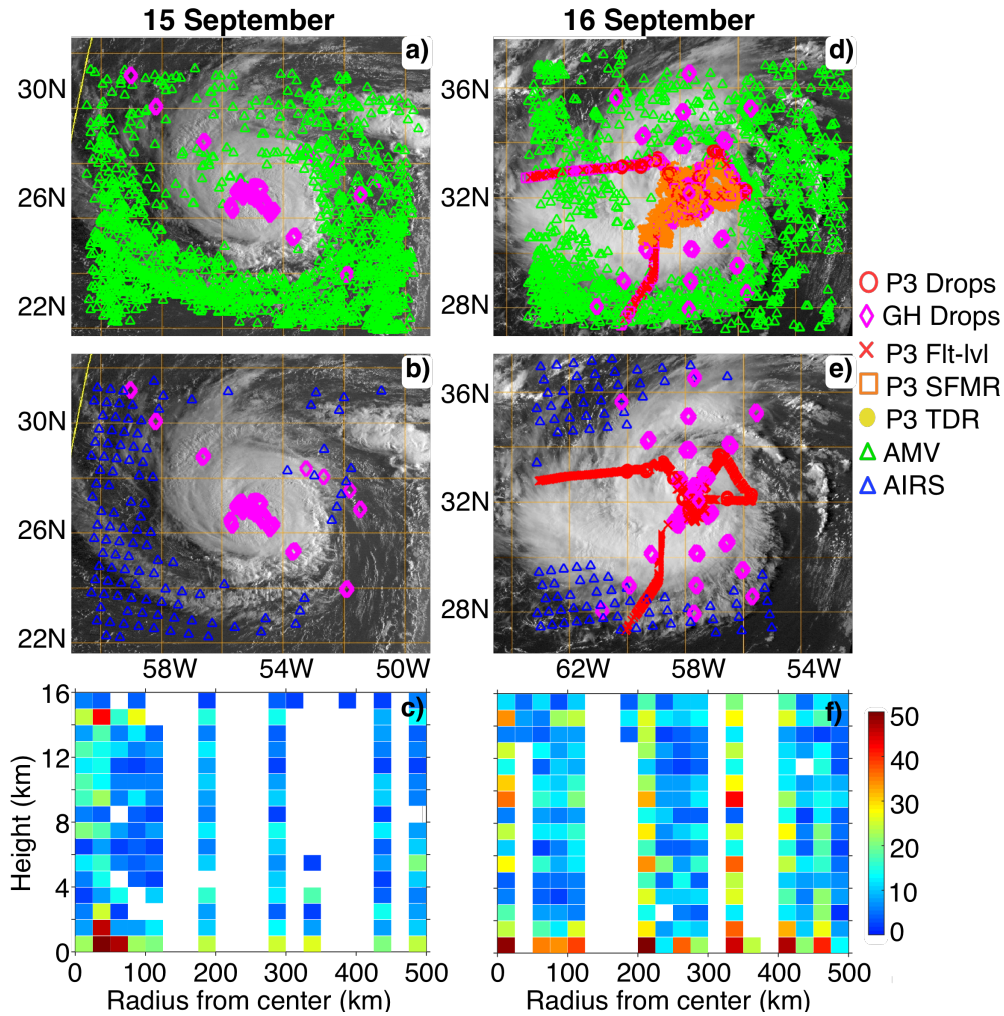


Fig. 1: Spatial distribution of assimilated observations overlaid on visible satellite imagery for the experiment All (including all available observations) centered at (a-c) 0600 UTC 15 September and (d-f) at 1800 UTC 16 September for (a,d) wind observations and (b,e) thermodynamic observations. [Visible imagery courtesy of Naval Research Laboratory, Monterey, CA.] (c,f) Number of GH dropwindsonde observations (purple diamonds in the (a-b, d-e)) within a bin of 25 km in radius and 1 km in height.

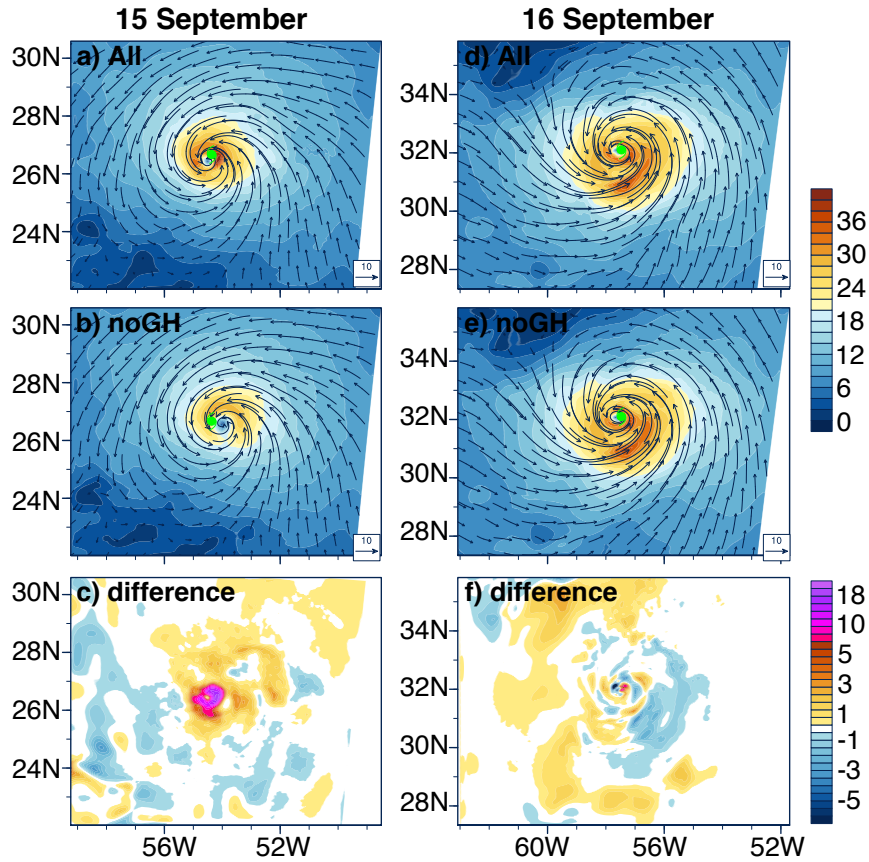


Fig. 2: 10-m wind vectors (m s^{-1} , wind speed shaded) of the final analysis in the experiment All and noGH and their differences (All-minus-noGH, wind fields in the experiment noGH is aligned to the center of the experiment All) at 0600 UTC 15 September (a-c) and 1800 UTC 16 September (d-f). The difference of the wind speed is contoured at 0.5 m s^{-1} intervals (-6 to 6 m s^{-1}) and at 2 m s^{-1} intervals (6 to 20 m s^{-1}). Observed Best Track positions are also indicated by the green hurricane symbols.

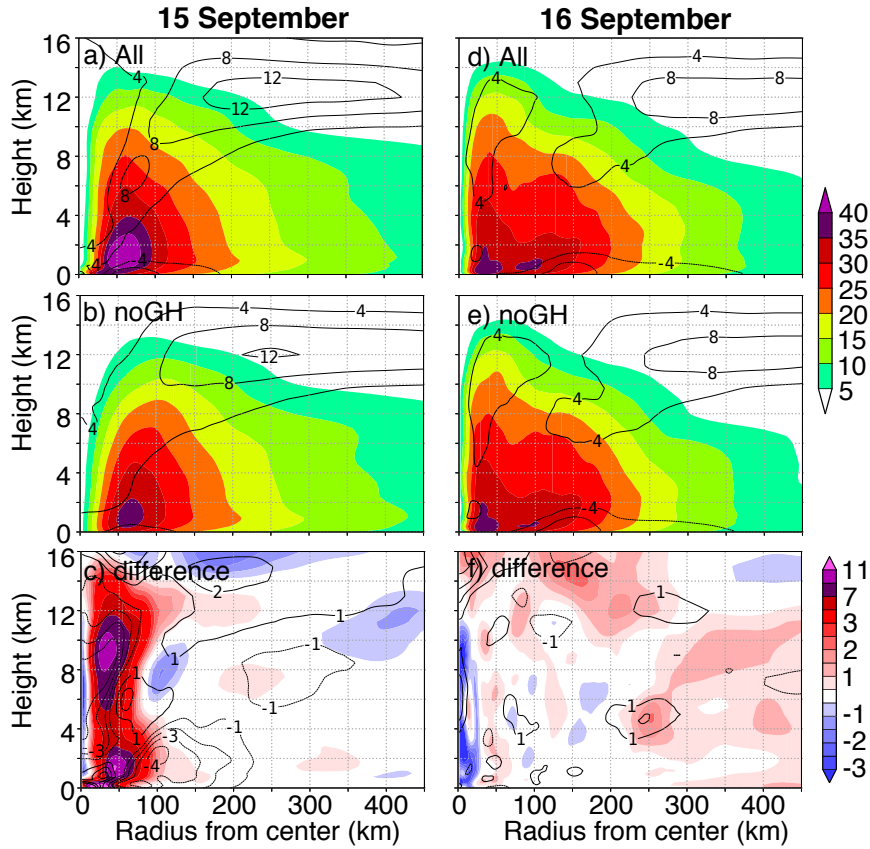


Fig. 3: Azimuthally averaged tangential wind speed (m s^{-1} , shaded) and radial wind speed (m s^{-1} , contours) of the final analysis from the experiment All (a,d) and noGH (b,e) and their differences (All-minus-noGH, c,f).

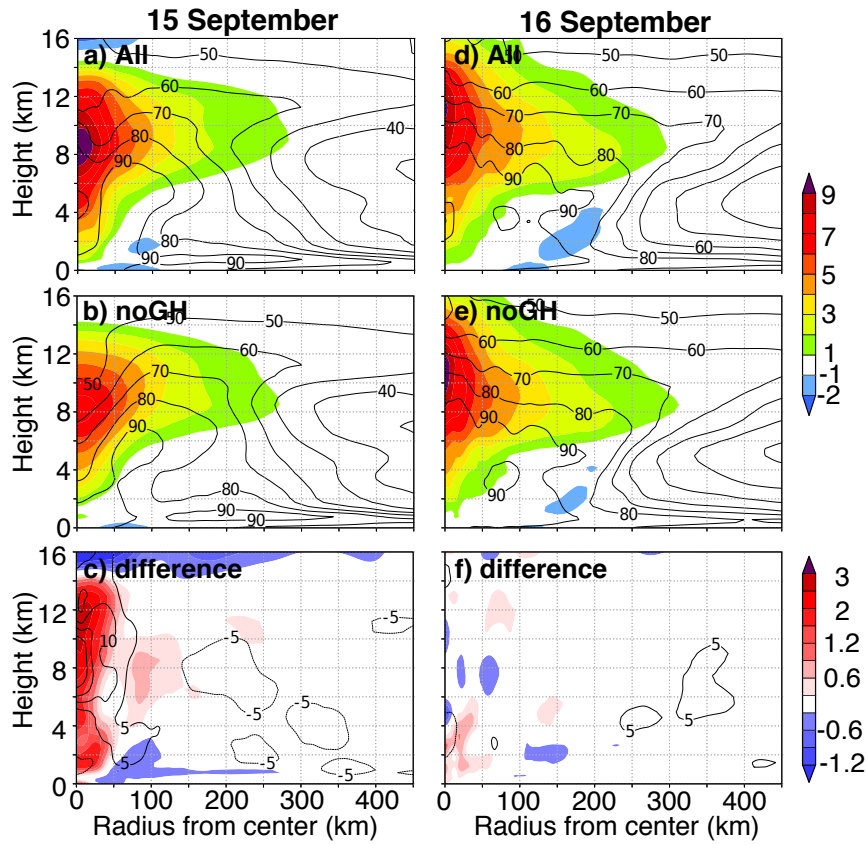


Fig. 4: As in Fig. 3 but for temperature anomaly (K, shaded) and relative humidity (% , contours).

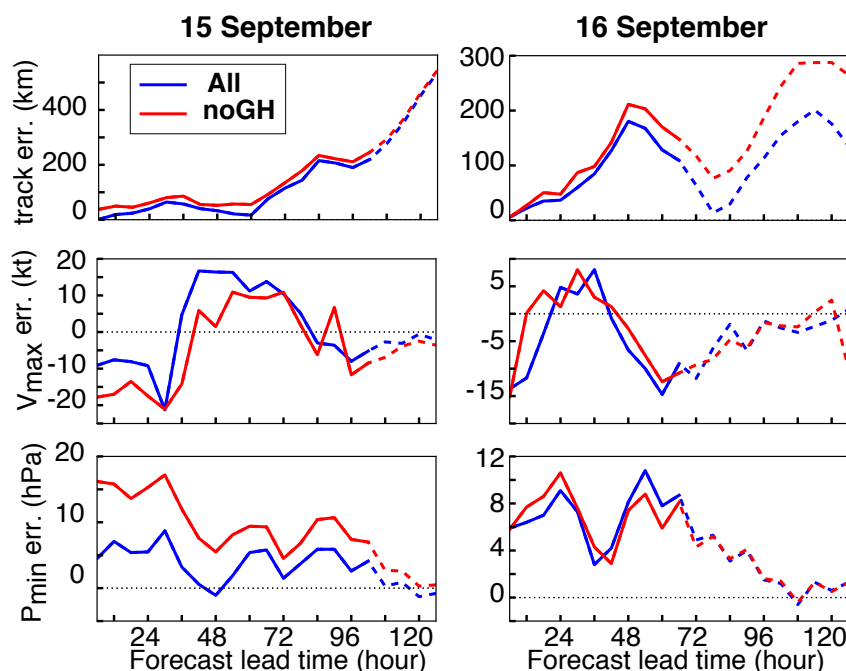


Fig. 5: Track error, maximum sustained 10-m wind speed error (V_{\max}), and minimum sea level pressure error (P_{\min}) compared to the observed Best Track from the deterministic forecasts in the experiments All and noGH initialized at 0600 UTC 15 September (left panel) and 1800 UTC 16 September 2014 (right panel). Dashed lines indicate that the storm is a remnant low in the Best Track estimates.

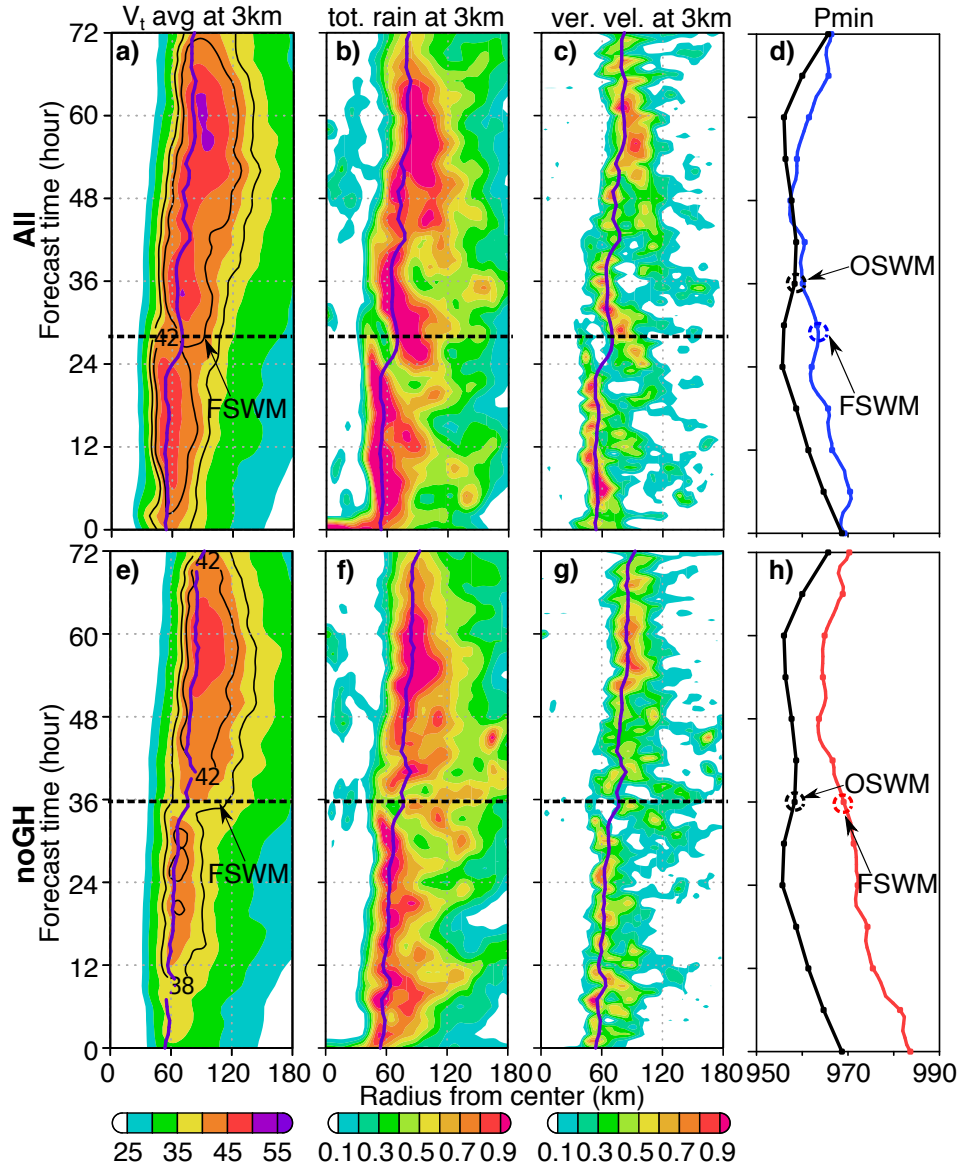


Fig. 6: Radius-time Hovmöller diagrams of (a,e) azimuthally averaged tangential wind speed layer-averaged between 2.4-km and 3.5-km altitudes (shaded with additional black contours at 42 and 38 m s^{-1}), (b,f) total cloud water content at 3-km altitude and (c,g) vertical velocity at 3-km altitude for the experiment All (a-c) and noGH (d-f) at hourly lead-time intervals initialized at 0600 UTC 15 September. The radius of maximum wind (RMW) at 1-km altitudes from both experiments are also shown in dark purple in (a-c) and (e-g). (d,h) Time evolution of the minimum sea level pressure (P_{\min}) from the experiment All (blue line), noGH (red line), and the best track estimates (black line). The black dashed lines in (a-c) and (e-g) mark the appearance of forecast secondary wind maximum (FSWM). Their corresponding time of observed secondary wind maximum (OSWM) is also shown in black dashed circles (d,h).

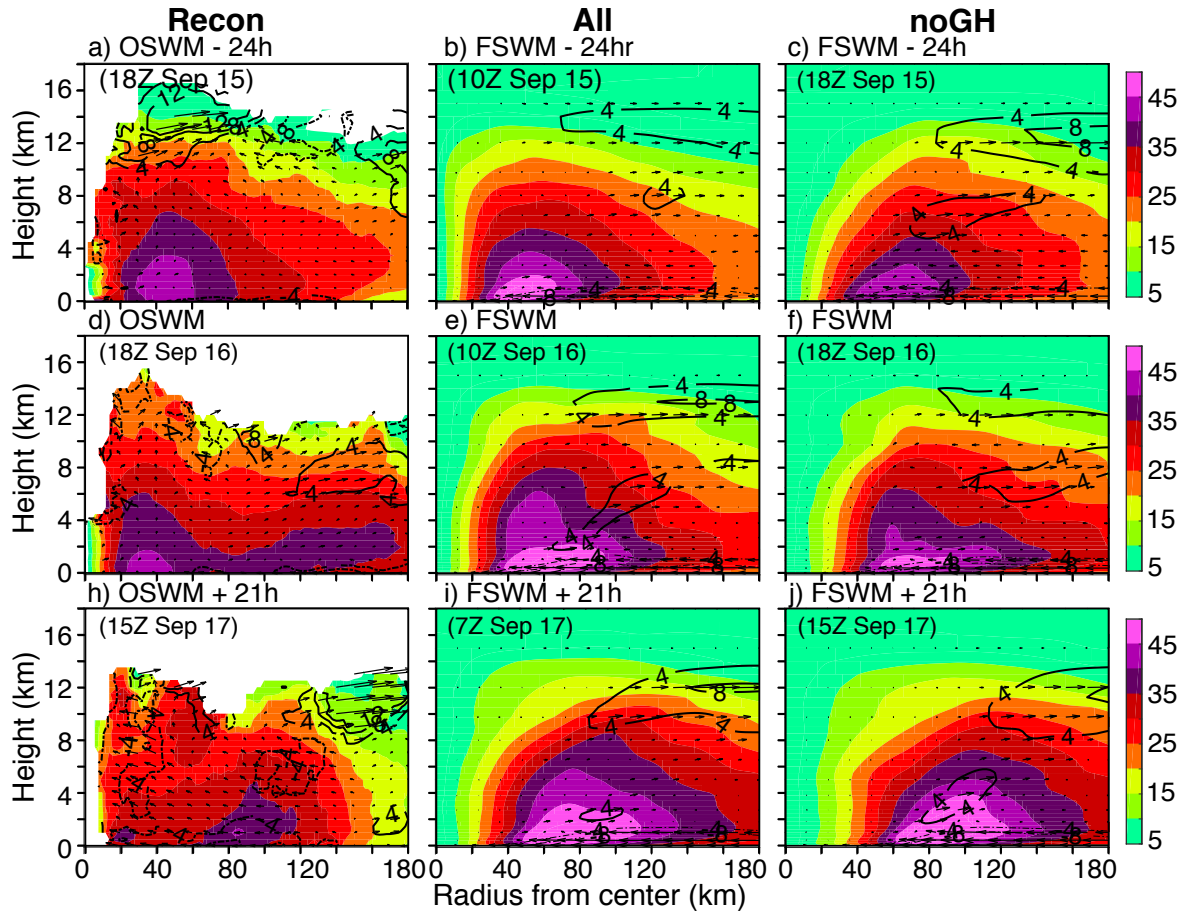


Fig. 7: Azimuthal mean of tangential wind speed (m s^{-1} , shaded), radial wind speed (m s^{-1} , contours) and secondary circulation (m s^{-1} , vectors of radial winds and vertical velocity) around observed secondary wind maximum (OSWM) and forecast secondary wind maximum (FSWM), and 24 hour before and 21 hour after of the OSWM and FSWM for Hurricane Edouard.

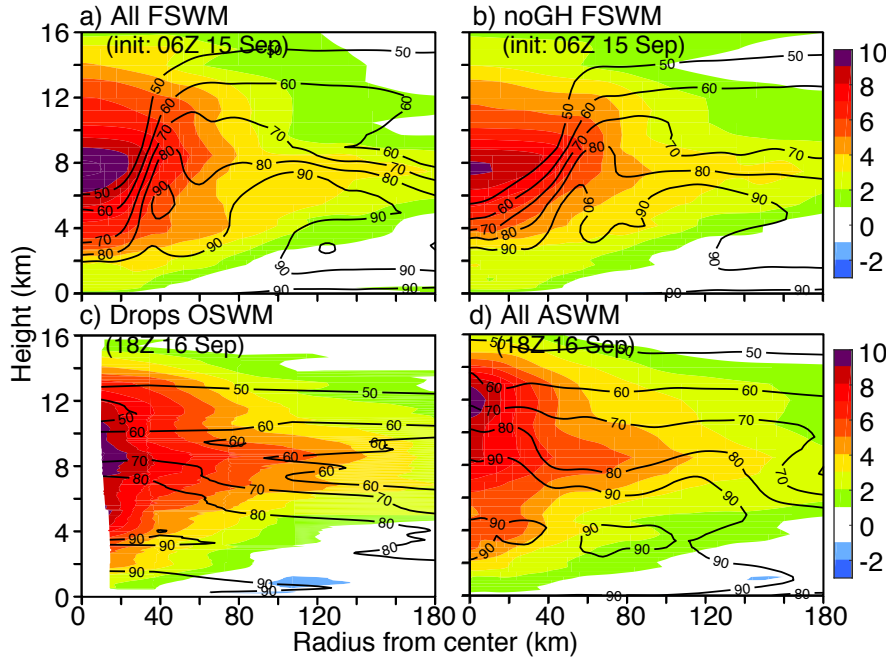


Fig. 8: Azimuthally averaged temperature anomaly (K, shaded) and relative humidity (%), contours) from (a) the experiment All and (b) noGH initiated from the analysis of the first case at 0600UTC 15 September at lead time when the appearance of forecast secondary wind maximum (FSWM) occurs, and (c) dropwindsonde composite ± 3 hour of 1800 UTC 16 September when observed secondary wind maximum (OSWM) occurs, and (d) the analysis of the secondary wind maximum (ASWM) from the case of 1800 UTC 16 September, 2014.

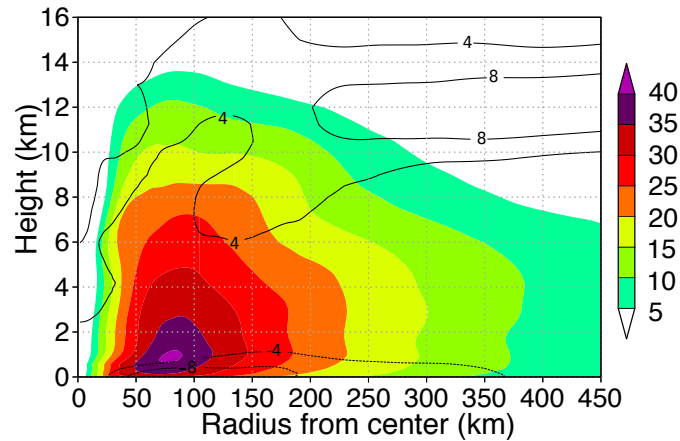


Fig. 9: Azimuthally averaged tangential wind speed (m s^{-1} , shaded) and radial winds (m s^{-1} , contours) from the analysis at 1800 UTC 16 September with P3 reconnaissance data denied.